SAND2022-11686C

Adaptive Control of Grid Forming Inverters for System Black Start

Oindrilla Dutta*, Tuofei Chen†, Deepak Ramasubramanian‡, and Evangelos Farantatos‡
* Sandia National Labs, Albuquerque, NM, USA
† Stanford University, Stanford, CA, USA
‡ Electric Power Research Institute, Palo Alto, CA, USA

***Abstract*—This work proposes a method of designing adaptive controllers for reliable and stable operation of a Grid-Forming Inverter (GFI) during black-start. Here, the characteristic loci method has been primarily used for guiding the adaptation and tuning of the control parameters, based on a thorough sensitivity analysis of the system over a desired frequency bandwidth. The control hierarchy comprises active-reactive (P-Q) power support, voltage regulation, current control, and frequency recovery over the sequence of various events during black-starting. These events comprise energization of transformers and different types of loads, alongside post-fault recovery. The developed method has been tested in a 75 MVA inverter system, which is simulated in PSCAD®. The inverter energizes static and induction motor loads, besides transformers. This system has also been subjected to a line-ground fault for validating the robustness of the proposed adaptive control structure in post-fault recovery.**

***Index Terms*—Adaptive control, Black-starting, Frequency recovery, Grid-forming inverter, and Voltage stability.**

I. Introduction

INVERTER based distributed energy resources have become vital for attaining the clean energy targets worldwide. With an increase in such inverter based resources (IBRs), there can potentially be a need to utilize them as designated black start resources. Black start is the process of power system restoration following an outage. Worldwide, restoration is treated as a critical aspect of power system operations and planning, for reducing interruptions to the economy and quality of life.

Transmission system operators plan a black start process based on the location and type of black start resources, presence of critical loads, and location of ties to neighboring systems [1]–[3]. The restoration process comprises initiation of generator start-up, followed by establishment of transmission network, load recovery, and system stabilization [4].

Steady-state and transient stability studies are traditionally performed to evaluate the restoration plans [5], [6]. Transient analysis is performed using conventional positive sequence software [7], [8], with the aim of: (1) Verifying dynamic performance of each unit in a power plant by monitoring the P-Q, voltage, and frequency; (2) Verifying no under frequency load shedding relays or generation relays are activated; (3) Determining the best frequency control mode (droop or isochronous). Studies are performed to validate these restoration plans in accordance with NERC EOP-005-2 R6 [9].

A universal guideline for conducting black-start is lacking, where analysis using electromagnetic transient (EMT) simulations are seldom adopted by the utilities. EMT simulation of a system with high penetration of IBRs is essential for determining its stability, when the IBRs participate in black-start. This is because black-start is characterized by a short-circuit strength of 0.0 when the first black-starting resource lights up that system, thereby making small changes in injected current potentially cause large changes in the terminal voltage of an IBR. This is a source of instability since fast controllers try to lock onto a fast moving system, in order to maintain rigid current control. The use of high bandwidth fast controllers to regulate a fast moving process drastically reduces its stability margin [10]. Thus, conventional phase locked loop (PLL) based controls may fail to operate in a 100% IBR system. In fact, PLL based control may be detrimental to system stability for obtaining inverter based generation levels of greater than 65% of the load served [11], [12]. Instead, controllers that allow the grid to view an inverter as a voltage source rather than a current source will be required [11], [13]. Such controllers would allow the magnitude and phase of the injected current to be largely uncontrolled if it is within the current limits of the power electronic components, thus allowing fast current injection. Although it can be inferred that such an operation would be impossible with a PLL, it has been shown in [14] that with careful design of the PLL based inverter control, the viability of operating a 100% inverter based system with only PLL based control architecture is indeed possible. This paves the way for adaptive primary control techniques that can perform prompt adjustment of control gains based on system conditions. Adaptation of the control gains must be performed within optimal limits, which can be determined by analysing stability of the system with respect to some disturbances.

In this work, an adaptive control architecture has been proposed for stable operation during energization of various loads, transformers and riding through a fault. The characteristic loci method has been adopted to evaluate the sensitivity of the system parameters to changes in the energization path. Performance of the proposed method has been demonstrated in a 75 MVA inverter-based black starting system, which has been studied in EMT domain using PSCAD®.

II. Overview of Control Design

This section provides an overview of the proposed control structure and its hierarchy, comprising P-Q support, frequency restoration, voltage stability and current control.

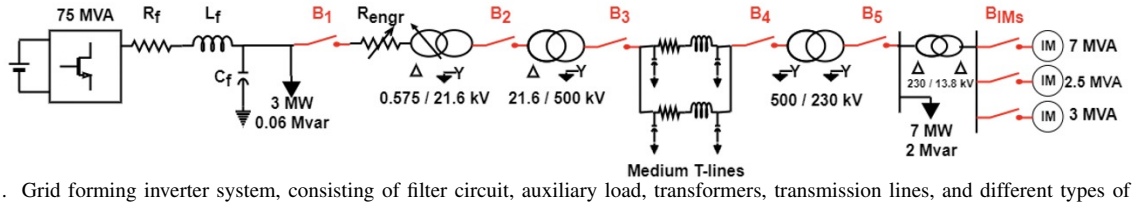

Fig. 1. Grid forming inverter system, consisting of filter circuit, auxiliary load, transformers, transmission lines, and different types of loads.

A. Active-reactive power (P-Q) control

This is the outermost layer in the control hierarchy, where P is regulated based on δ-P droop. However, unlike conventional droop, the control parameters are adaptive based on the states of the system. The controller at this level also generates voltage reference (V_{ref}), as a function of both P and Q.

The IBR being disconnected from the grid, requires an efficient frequency controller that is capable of providing quick recovery from disturbances. Here, a synchronous reference frame phase-locked loop (SRF-PLL) has been used for that.

B. Voltage control

This is the second level in the control hierarchy, whose primary task is accurate tracking of V_{ref} from the outermost layer and providing set-points to the current controller. It is also provisioned with a power system stabilizer for damping out oscillations arising from motor loads. The control parameters are adapted for adjusting to changes in the system.

C. Current Control

This is the innermost controller in the hierarchy and receives current set-points from the higher-level controllers. Being in the lowest level, this controller must be the fastest among the three levels. Hence, the control parameters are designed for a wider bandwidth of operation, without any adaptive gains.

III. System Under Study

The case study comprises a 75 MVA inverter that black starts a grid by sequentially energizing various types of loads and transformers, as illustrated in Fig. 1. The inverter is connected to a 3MW auxiliary load and the voltage and frequency control loops activate at $t = 1.5s$ *(1)*. The sequence of events thereafter involves energizing different components such as: *(2)* a 0.575/21.6 kV transformer at 6s; *(3)* a 21.6/500 kV transformer at 7s; *(4)* a medium T-line at 12s; *(5)* at 25s a 7MW constant I-load pickup along with three induction motor loads of *(6)* 7 MVA, *(7)* 2.5 MVA and *(8)* 3 MVA capacities. *(9)* At 100s, a 80ms line-ground fault is applied at the T-line.

IV. Detailed Control Design

This section elaborates on the design approach for adapting the sensitive parameters in the individual control layers.

A. Current Controller

The current, (I), through the inverter filter (Fig. 2) is decoupled into its direct axis (d) and quadrature axis (q) components, which are being regulated to accurately follow the references received from the higher level controllers.

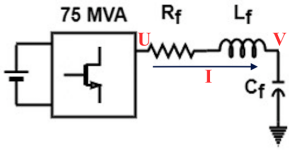

Fig. 2. The inverter under study and its filter circuit.

1) Decoupled Control Design: The control method for the $3-\phi$ I through the inverter filter, after being transformed to its *d-q* components, is illustrated in Fig. 3. The corresponding transfer function is shown in (1).

$$I_{d/q} = \frac{GK_{d/q}}{1+GK_{d/q}} I_{d/q-ref} - \frac{G}{1+Gd/q} V_{d/q} + \frac{\omega L_f G}{1+GK_d} I_{q/d} \tag{1}$$

where, $I_{d/q}$ are the d/q components of the measured $3-\phi$ I, $I_{d/q-ref}$ are the d/q current references, $V_{d/q}$ are the d/q components of the measured voltage across the filter capacitor, C_f. R_f and L_f are the filter parameters of the inverter, where

$$G = \frac{1}{R_f + sL_f}$$

$K_{d/q}$ is either a proportional (P) or a proportional-integral (PI) gain. The choice of $K_{d/q}$ is crucial to the stability margin of

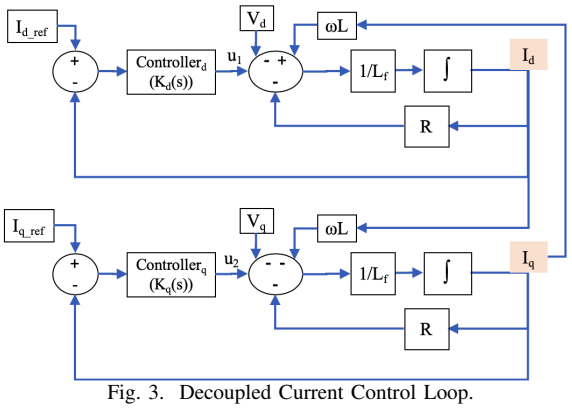

Fig. 3. Decoupled Current Control Loop.

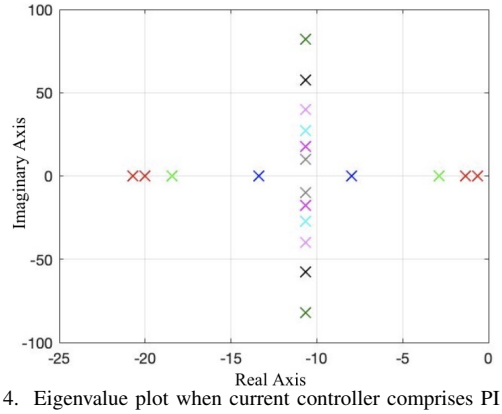

Fig. 4. Eigenvalue plot when current controller comprises PI gains.

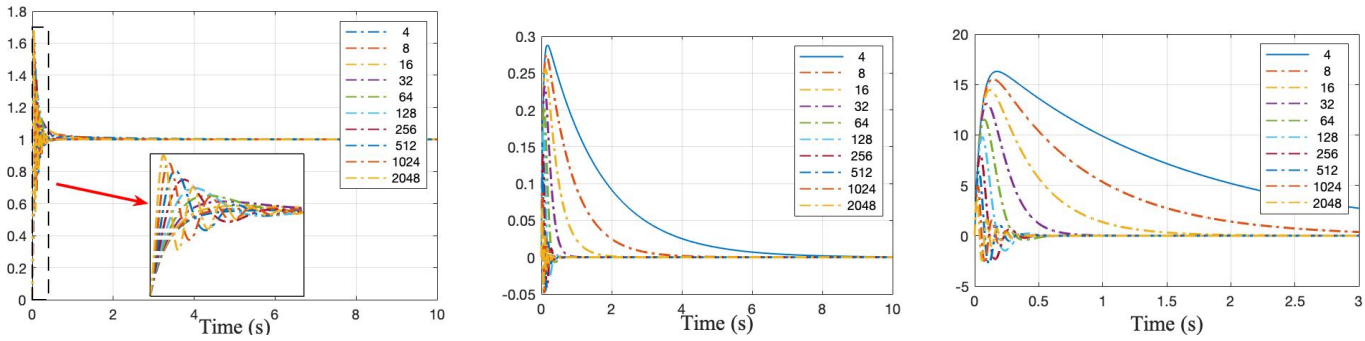

(a) I_d with respect to I_{d-ref}, (b) I_d with respect to V_d, (c) I_d with respect to I_q,

Fig. 5. Step response of I_d with respect to I_{d-ref}, I_q and V_d , when a fixed proportional gain and a varying integral gain are used for current control.

the system since increasing $K_{d/q}$ ascertains accurate tracking of I_{d-ref} by I_d, as demonstrated by (2).

$$\lim_{K_{d/q}\to\infty} I_d = [\mathrm{I}] * I_{d/q-ref} + 0 + 0 \tag{2}$$

However, a very high value of $K_{d/q}$ can also push the system towards instability, and hence this necessitates careful tuning.

2) Stability Analysis: The eigenvalues pertaining to (1) with K_d as a P-gain, are evaluated by varying K_d from 0.2 to 3276. Although the eigenvalues become more negative with increasing P-gain, a dominant pole always exists at the origin. The corresponding step responses of I_d, with respect to I_{d-ref}, I_q and V_d show an over-damped response and a considerable steady state error in the response of I_d with respect to I_q. Consequently, an integral-gain has been added to a P-gain of 3.2, where the integral gain is varied from 2 to 2048. The resulting eigenvalues and step responses are illustrated in Figs. 4 and 5, respectively. Fig. 4 shows that the dominant eigenvalues have shifted to the left of the imaginary axis and the step responses show improved performance in terms of rise/settling times, peak values, and steady state errors. Since the current controller must be the fastest in the control hierarchy, the integral gain has been chosen to be 32.

B. Voltage Controller

Fig. 6 shows the control structure for regulating the voltage and stabilizing frequency oscillations.

1) Sensitivity to Reference Input: V_{ref} adapts based on the $P-Q$ variation in the system, as shown in (3) [15].

$$V_{ref} = V_{nom} + K_{PQ}[m_Q Q + m_P P] \tag{3}$$

Since the inverter system is primarily voltage controlled and lacking in rotational inertia, a $V-Q$ droop is insufficient in reflecting the voltage condition in this case study. The parameters in (3) are constant and tuned such that the voltage

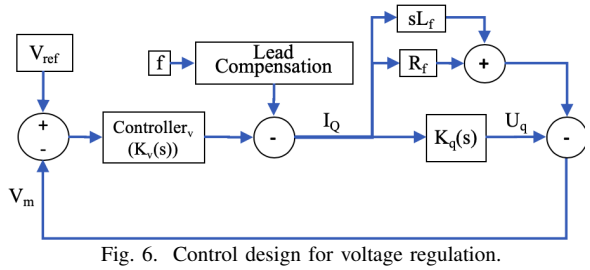

Fig. 6. Control design for voltage regulation.

remains within its minimum/maximum limits during worst case scenario that is specific to the system.

The transfer function of the measured output voltage (V_m) with respect to V_{ref} is presented in (4),

$$V_m = \frac{K_v(s)[Kq(s) - R_f - sL_f]}{1 + K_v(s)[Kq(s) - R_f - sL_f]} V_{ref} \tag{4}$$

where $K_q(s) = K_{pi} + K_{ii}/s$, is obtained from the current control design in Section IV-A, and K_v is the control gain of the voltage controller. The response of V_m with $K_v(s)$ as a P-gain (K_{pv}), evaluated using (5), is presented in Fig. 7.

$$V_m = \frac{s^2 K_{pv} L_f + sK_{pv}(R_f - K_{pi}) - K_{pv}K_{ii}}{s^2 K_{pv} L_f + s[K_{pv}(R_f - K_{pi}) - 1] - K_{pv}K_{ii}} V_{ref} \tag{5}$$

The step response shows instability when a P-gain is used for voltage regulation. The response of V_m with $K_v(s)$ as an integral gain (K_{iv}), evaluated using (6), is presented in Fig. 8.

$$V_m = \frac{s^2 K_{iv} L_f + sK_{iv}(R_f - K_{pi}) - K_{iv}K_{ii}}{s^2 (K_{iv} L_f - 1) + sK_{iv}(R_f - K_{pi}) - K_{iv}K_{ii}} V_{ref} \tag{6}$$

It is evident from the Fig. 8 that an integral gain provides accurate tracking and fast response of the variable reference. However, the log-magnitude plot also shows a small bandwidth of operation, which implies poor tracking and slow response at higher order frequencies. This may introduce voltage instability in the form of oscillations when motor loads are energized by the inverter [16], [17]. Hence, the voltage controller has been equipped with an adaptive frequency compensation loop, as illustrated in Fig. 9. The adaptation of the pole (at $-1/T$)

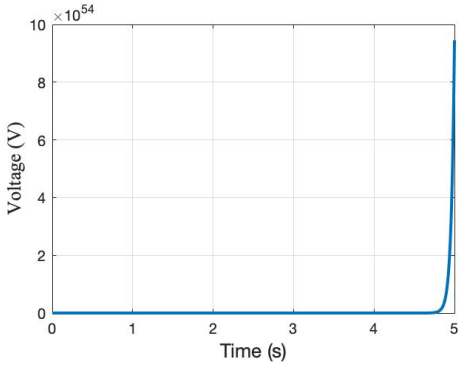

Fig. 7. Step responses of V_m with respect to V_{d-ref} when P-gain is used for voltage control

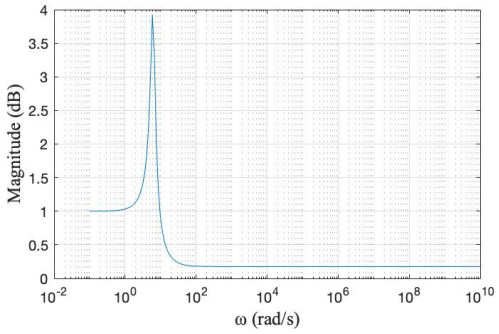

(a) Log-magnitude response of V_m with respect to V_{d-ref},

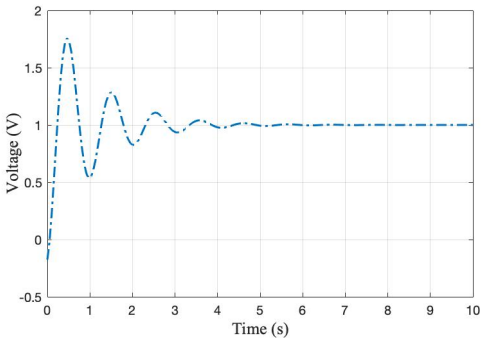

(b) Step response of V_m with respect to V_{d-ref},

Fig. 8. Frequency and Step responses of V_m with respect to V_{d-ref} when integral gain is used for voltage control.

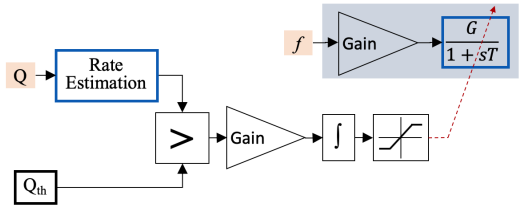

Fig. 9. Frequency compensation for voltage controller.

in the compensation loop is based on the reactive power profile during the starting of an induction motor, which is characterised by a steep rise followed by a gradual descent. Thus, T is introduced into the loop when the rate of decrease of reactive power exceeds a threshold (Q_{th}), and its value is an integral function of the reactive power (Q).

C. Active Power Controller

In the active power controller shown in Fig. 10, active power (P_{ord}) is modulated based on the deviation of frequency (f_m) from its nominal value (f_{ref}) and is responsible for providing I_{d-ref} (I_p) to the current controller after being divided by V_m. The frequency, being a function of V_q, makes the regulation of P_{ord} a coupled control problem, as expressed by (7).

$$V_p\sqrt{V_p^2+V_q^2} = \left[(f_{ref}-f_m)\left(\frac{K_w}{60}+\frac{K_\delta G}{sT(1+sT_1)}\right)+ P_{ref}-\delta_{ref}\frac{K_\delta G}{1+sT}\right]\left[K_p(s)-R_f-sL_f\right] \tag{7}$$

Analysis of (7) with $V_q = 0$, which also implies $f_m = f_{ref}$, provides a small signal response of V_d with respect to P reference (P_{ref}) and phase angle refrence (δ_{ref}) when frequency is stable, as shown in (8) and (9), respectively.

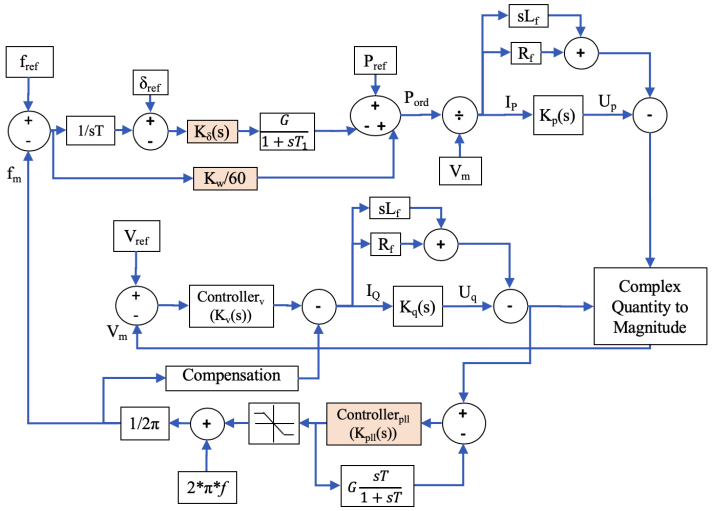

Fig. 10. Closed-loop control structure of the active power controller.

$$V_d\frac{\partial V_d}{\partial P_{ref}} = \frac{K_{ii}+(K_{ip}-R_f)s-L_f s^2}{2s} \tag{8}$$

$$V_d\frac{\partial V_d}{\partial \delta_{ref}} = \frac{K_\delta G\left[K_{ii}+s(K_{ip}-R_f)-s^2L_f\right]}{Ts^2+s} \tag{9}$$

The log magnitude analysis of (9) at the equilibrium point of $V_p = 1$ p.u. ascertains a stable operation within the necessary bandwidth. Performance of the active power controller, during frequency variations that may be initiated by change in loading scenario and its post-fault recovery, can be evaluated by analyzing (7) with $V_p = 0$. The characteristic loci method has been adopted here, where the coupling of f with other control parameters is of importance and is shown in (10).

$$f = f_{ref}+\frac{1}{\frac{K_w}{60}+\frac{K_\delta G}{sT(1+sT_1)}}P_{ref}-\frac{GK_\delta}{\frac{K_w(1+sT_1)}{60}+\frac{GK_\delta}{sT}}\delta_{ref} \tag{10}$$

Log magnitude analysis of (10) show that the coupling between f and P_{ref} is primarily shaped by the parameter K_w and increasing this gain provides improved damping of the output for a wide range of frequencies. The impact of varying the gain K_δ on the coupling between f and δ_{ref} show that although K_δ provides damping to the output, however, the impact is limited to the lower frequencies, where f is already stable as explained in prior discussion. Consequently, the

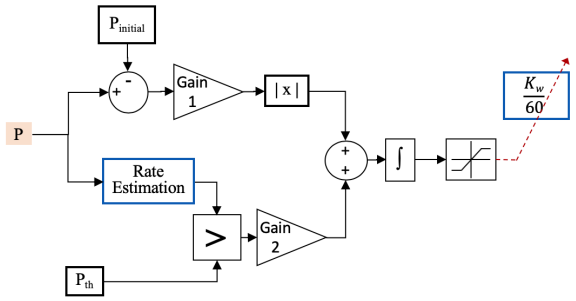

Fig. 11. Adaptation of the parameter K_w as a function of active power.

parameter K_w has been made adaptive based on the active power demand and its rate of change, as demonstrated by Fig. 11. The increased gain provides damping to frequency oscillations when the active power demand sharply increases and exceeds that of the auxiliary load.

V. Simulation Results

The system along with the sequence of events as depicted in Section III, has been simulated in PSCAD® for 120 seconds. The corresponding voltage and frequency are shown in Figs. 12 and 13, respectively. Fig. 12 shows the voltages measured at three different points in the energization path. Besides successful energization, this figure shows that the voltage oscillations corresponding to events *(6)*, *(7)*, and *(8)* have been satisfactorily damped. Also, the control architecture was able to recover the voltage after the L-G fault in event (9). Fig. 13 shows that the frequency drops to 59.88 Hz after energization of the 3 MVA motor load, but recovers thereafter, thereby avoiding violation of the frequency limits.

VI. Conclusion

In this work, a method of designing adaptive controllers for a grid-forming inverter that black starts a network has been developed. The effectiveness of the method has been demonstrated with a 75 MVA inverter based black starting system that energizes transformers, static and motor loads, and recovers the system frequency and voltage after an L-G fault.

The analysis provided parameter gains with a wide bandwidth of operation for decoupled current control design. Our evaluation of the voltage control loop showed the requirement of power system stabilizers with adaptive time constant for damping out oscillations arising from motor loads. Besides, the active power support required adaptive parameter gains for achieving stable and reliable operation of the system.

The simulation results using PSCAD® illustrate the system voltage and frequency during the different sequence of events in the energization process. These results validate that appropriate regulation of voltage during the sequence and frequency restoration after the fault have been achieved with the proposed control architecture.

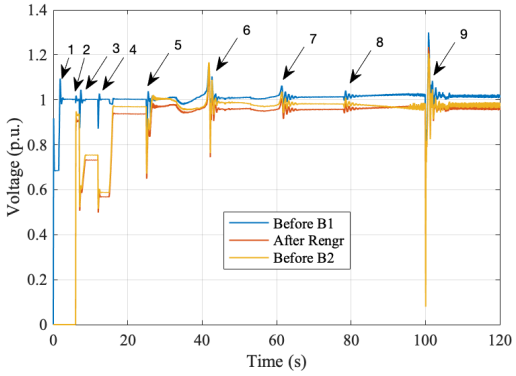

Fig. 12. System voltage at three different points in the energization path.

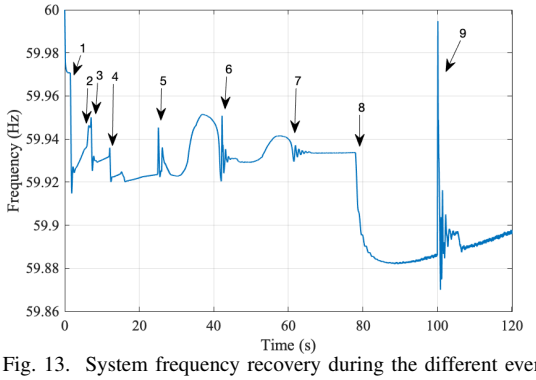

Fig. 13. System frequency recovery during the different events.

References

[1] M. Adibi, P. Clelland, L. Fink, H. Happ, R. Kafka, J. Raine, D. Scheurer, and F. Trefny, "Power system restoration - a task force report," *IEEE Transactions on Power Systems*, vol. 2, no. 2, pp. 271–277, 1987.

[2] M. Sforna and V. Bertanza, "Restoration testing and training in italian iso," *IEEE Transactions on Power Systems*, vol. 17, no. 4, pp. 1258–1264, 2002.

[3] N. Saraf, K. McIntyre, J. Dumas, and S. Santoso, "The annual black start service selection analysis of ercot grid," *IEEE Transactions on Power Systems*, vol. 24, no. 4, pp. 1867–1874, 2009.

[4] W. Sun, C.-C. Liu, and S. Liu, "Black start capability assessment in power system restoration," in *2011 IEEE Power and Energy Society General Meeting*, 2011, pp. 1–7.

[5] Y. Liu, R. Fan, and V. Terzija, "Power system restoration: a literature review from 2006 to 2016," *Journal of Modern Power Systems and Clean Energy*, vol. 4, no. 3, pp. 332–341, 2016.

[6] M. Nagpal, T. G. Martinich, Z. Jiao, S.-H. Manuel, H. A. Zhang, and A. Alimardani, "Lessons learned from a regional system blackout and restoration in bc hydro," *IEEE Transactions on Power Delivery*, vol. 33, no. 4, pp. 1954–1961, 2018.

[7] L. Sun, C. Peng, J. Hu, and Y. Hou, "Application of type 3 wind turbines for system restoration," *IEEE Transactions on Power Systems*, vol. 33, no. 3, pp. 3040–3051, 2018.

[8] A. P. Asensio, S. A. Gómez, J. L. Rodriguez-Amenedo, and M. Á. Cardiel-Álvarez, "Decentralized frequency control for black start of full-converter wind turbines," *IEEE Transactions on Energy Conversion*, vol. 36, no. 1, pp. 480–487, 2020.

[9] "System restoration from blackstart resources," Standard, Nov. 2013. [Online]. Available: https://www.nerc.com/pa/Stand/Reliability/20Standards/EOP-005-2.pdf

[10] D. Ramasubramanian *et al.*, "Positive sequence voltage source converter mathematical model for use in low short circuit systems," *IET Generation, Transmission Distribution*, vol. 14, no. 1, pp. 87–97, 2020.

[11] M.-S. Debry, G. Denis, and T. Prevost, "Characterization of the grid-forming function of a power source based on its external frequency smoothing capability," in *2019 IEEE Milan PowerTech*, 2019, pp. 1–6.

[12] R. Ierna, J. Zhu, A. Roscoe, M. Yu, A. Dyśko, C. Booth, and H. Urdal, "Effects of vsm convertor control on penetration limits of non-synchronous generation in the gb power system," in *15th Wind Integration Workshop on Large-Scale Integration of Wind Power into Power Systems as well as on Transmission Networks for Offshore Wind Power Plants*, Nov. 2016.

[13] D. Ramasubramanian, Z. Yu, R. Ayyanar, V. Vittal, and J. Undrill, "Converter model for representing converter interfaced generation in large scale grid simulations," *IEEE Transactions on Power Systems*, vol. 32, no. 1, pp. 765–773, Jan 2017.

[14] D. Ramasubramanian and E. Farantatos, "Viability of synchronous reference frame phase locked loop inverter control in an all inverter grid," in *2020 IEEE Power Energy Society General Meeting (PESGM)*, 2020, pp. 1–5.

[15] E. Rokrok and M. E. H. Golshan, "Adaptive voltage droop scheme for voltage source converters in an islanded multibus microgrid," *IET generation, transmission & distribution*, vol. 4, no. 5, pp. 562–578, 2010.

[16] P. Kundur, "Power system stability," *Power system stability and control*, pp. 7–1, 2007.

[17] R. Yan and T. K. Saha, "Investigation of voltage stability for residential customers due to high photovoltaic penetrations," *IEEE transactions on power systems*, vol. 27, no. 2, pp. 651–662, 2012.